

Evolution of the Microstructure of Laser Powder Bed Fusion Ti-6Al-4V During Post-Build Heat Treatment



D.W. BROWN, V. ANGHEL, L. BALOGH, B. CLAUSEN, N.S. JOHNSON,
R.M. MARTINEZ, D.C. PAGAN, G. RAFAILOV, L. RAVKOV, M. STRANTZA,
and E. ZEPEDA-ALARCON

The microstructure of additively manufactured Ti-6Al-4V (Ti64) produced by a laser powder bed fusion process was studied during post-build heat treatments between 1043 K (770 °C) and just above the β transus temperature 1241 K (1008 °C) *in situ* using high-energy X-ray diffraction. Parallel studies on traditionally manufactured wrought and annealed Ti64 were completed as a baseline comparison. The initial and final grain structures were characterized using electron backscatter diffraction. Likewise, the initial texture, dislocation density, and final texture were determined with X-ray diffraction. The evolution of the microstructure, including the phase evolution, internal stress, qualitative dislocation density, and vanadium distribution between the constituent phases were monitored with *in situ* X-ray diffraction. The as-built powder bed fusion material was single-phase hexagonal close packed (to the measurement resolution) with a fine acicular grain structure and exhibited a high dislocation density and intergranular residual stress. Recovery of the high dislocation density and annealing of the internal stress were observed to initiate concurrently at a relatively low temperature of 770 K (497 °C). Transformation to the β phase initiated at roughly 913 K (640 °C), after recovery had occurred. These results are meant to be used to design post-build heat treatments resulting in specified microstructures and properties.

<https://doi.org/10.1007/s11661-021-06455-7>

© The Minerals, Metals & Materials Society and ASM International 2021

I. INTRODUCTION

METAL additive manufacturing (AM) is a rapidly developing processing pathway that produces components by selective fusion of feedstock material on demand to build a specified geometry.^[1–4] The process typically results in initial rapid solidification and quenching of the deposited material^[4–6] followed by many repeated thermal cycles during deposition of subsequent layers of material^[7,8] producing novel, high-energy, metastable microstructures.^[5,9,10] Titanium alloys are an attractive material for AM because the process can greatly reduce material waste and the high cost of machining. Ti-6Al-4V (Ti64) has been one of the most utilized titanium alloys in, for example, the

aerospace industry because of its combination of low density, high strength, and corrosion resistance.^[11]

Traditional processing of Ti64 relies on relatively slow cooling fabrication processes, such as casting, resulting in equilibrium microstructures composed of roughly 94 volume percent α -phase (hexagonal close packed, HCP) and 6 volume percent β -phase (body-centered cubic, BCC).^[11,12] The slow cooling rate during casting enables diffusion of V, the β stabilizer, primarily into the minority β -phase leaving the α -phase enriched in Al.^[11–15] The advantageous properties of Ti64, in particular the ductility, depend on this equilibrium microstructure. The high cooling rates associated with most AM processing routes, however, result in martensitic transformation direct from the high-temperature β -phase to an acicular vanadium supersaturated α' -phase^[1,8,14,16] which has the same HCP crystal structure as the α -phase but larger lattice parameters.^[17] While the as-built α' quite frequently has superior strength when compared to wrought Ti64, it also has reduced ductility.^[18] Thus, much work has been done to either manipulate the manufacturing process^[8,14,18] or devise heat treatments^[17,19–21] to control the final microstructure and optimize the properties of AM Ti64.

There has been considerable work recently to examine microstructural evolution *in situ* during simulated

D. W. BROWN, V. ANGHEL, B. CLAUSEN, N. S. JOHNSON, R. M. MARTINEZ, and E. ZEPEDA-ALARCON are with the Los Alamos National Laboratory, Los Alamos, NM, 87545. Contact e-mail: dbrown@lanl.gov. L. BALOGH and L. RAVKOV are with the Queens University, Kingston, Ontario K7L 3N6, Canada. D. C. PAGAN is with the Penn State University, University Park, PA, 16802. G. RAFAILOV is with Nuclear Research Center of the Negev, PO Box 9001, Beer Sheva, 84190, Israel. M. STRANTZA is with the Lawrence Livermore National Laboratory, 7000 East Ave, Livermore, CA 94550.

Manuscript submitted March 29, 2021; September 3, 2021.

Article published online October 4, 2021

AM^[22–24] or similar high solidification rate processes.^[13,25,26] However, the high cooling rates associated with AM, estimated at 10^3 K/s^[27] to 10^6 K/s^[28] depending on the process type, demand measurement rates of kHz to MHz. This, in turn, forces sacrifices in data quality that limits the amount of quantitative microstructural information (e.g., phase fraction, texture, internal stress) that can be gleaned from the diffraction data.^[22,24,27,29] In contrast, relatively few *in situ* studies of the evolution of the metastable AM microstructure during post-build heat treatments are to be found in the literature^[15,30–32] despite the fact that the relatively slow kinetics during heat treatments often enable quantitative determination of relevant microstructural parameters. Hysteretic lattice parameter expansion was observed during *in situ* heat treatment of shaped metal deposited Ti64 using low energy (8 keV; penetration depth ~ 0.01 mm) X-rays.^[15] However, the evolution of the α and β phase fractions was not obtainable. In contrast, neutron diffraction measurements reveal hysteretic behavior of the α and β phase fractions in Selective Laser Melted Ti64 during heating treatment, but do not report hysteresis of the lattice parameters, possibly because the results were averaged over all spatial and crystal orientations.^[31] Neutron diffraction measures on Ti64, while penetrating into the bulk of the material, are very slow due to the low coherent neutron scattering cross section of Ti. The advent of high-energy (> 60 keV) X-ray beamlines at 3rd generation synchrotron sources provides an optimal platform to study the microstructural evolution of AM Ti alloys during heat treatment because it enables both bulk penetration and the ability to collect diffraction patterns sufficient for qualitative microstructural analysis at frequencies of order 1 Hz^[27] or potentially higher.

The current work utilizes *in situ* high-energy X-ray diffraction techniques at the Cornell High-Energy Synchrotron Source (CHESS) to monitor the microstructural evolution during heat treatment of Laser Powder Bed Fusion^[33] (L-PBF) Ti64. For instance, the evolution of the β -phase volume fraction, v_β , is tracked quantitatively through thermal cycles to 1043 K (770 °C), 1113 K (840 °C), and 1281 K (1008 °C) and return to room temperature. This probe of the process-structure relationship is aimed toward developing models to be utilized to design post-build thermal treatments of AM Ti64.

II. EXPERIMENTAL METHODS

A. Sample Preparation

Samples for *in situ* heat treatment, summarized in Table I, were harvested from a “bridge” build structure with overall dimensions of 9 mm tall (Build Direction: BD) \times 5 mm thick (Transverse Direction: TD) \times 21 mm long (Longitudinal Direction: LD) described in a previous publication.^[34,35] The bridge-shaped Ti64 specimen was produced via L-PBF using a Concept Laser M2 machine[®]. A laser power of 100 W, scan speed of 600 mm/s, and beam size of 54 μ m were used, along with

layer thickness of 30 μ m and hatch spacing of 105 μ m, resulting in an input volumetric energy density^[2] of 52.9 J/mm. Three of the samples studied herein (PBF1) were removed from a bridge made with a continuous track laser scanning strategy, alternating layers between the LD and TD. The fourth sample (PBF2) came from a bridge made with the same parameters, but the continuous laser tracks were rotated 45 deg with respect to the LD and TD in the build plane. The samples, nominally 4 \times 3 \times 0.8 mm (BD \times TD \times LD, respectively), were electro-discharge machined, closely spaced, from the center of a leg of the bridge, as indicated schematically in Figure 1. The observed residual stress in the region of the bridge component from which the samples were removed was, while not zero, relatively uniform [Strantzis, 2021 #2472] and symmetric with respect to the other leg. The samples were chemically etched to remove the re-cast layer from the sample surface. During heat treatment, the samples were held loosely in a 5 mm \times 4 mm \times 1 mm pocket milled into a 316L stainless steel plate and subsequently covered with a second 316L plate. The sample container was sealed with an electron beam weld circumnavigating the sample position roughly 5 mm from the edge of the pocket, resulting in an evacuated space around the sample protecting the Ti64 sample from oxidation during the experiment, see the schematic in Figure 1. Following the heat treatment, the samples were easily removed from the container for subsequent microscopy by cutting inside of the weld seal. Examination of the samples after the *in situ* heat treatment experiments indicated no surface oxidation of the samples.

B. Microscopy

The samples were prepared for Electron Backscatter Diffraction (EBSD) as follows. Sample preparation consisted of grinding on SiC paper with increasingly fine grit, followed by mechanical polishing using 0.3 μ m α alumina slurry and then a mixture of 10:1 by volume of 0.04 μ m colloidal silica and hydrogen peroxide. The as-polished surface was etched lightly by immersion in a reagent containing 25 ml water, 12.5 ml nitric acid, and 2.5 ml hydrofluoric acid. EBSD measurements were performed on a Phillips FEI XL30 FEG SEM or on a Thermo Scientific Apreo SEM, along with TSL Data Collection and Analysis software. EBSD data were acquired at high magnification using a voltage of 20 kV and a step size of 0.2 μ m.

C. X-ray Diffraction Measurement

The *in situ* heating measurements were completed on the newly constructed Forming and Shaping (FAST) beamline at the Cornell High-Energy Synchrotron Source. Figure 1 shows a schematic of the experimental setup. The steel sample container was mounted from an insulating BN rod such that the sample was at the diffractometer center within the hot zone of the coils of an induction furnace. The induction coil was mounted with the axis vertical and split to penetration of the incident and diffracted X-rays. A type K thermocouple

Table I. Sample Nomenclature, Nominal Heat Treatment Temperature, β Phase Fraction (v_β and Vanadium Concentration in β Phase ($[V_\beta]$) in the Initial Condition, When the Heat Treatment (HT) Temperature is Reached, When HT Completes and Upon Return to Room Temperature

Sample Name	HT Temp. K(C)	Initial v_β	Reach HT v_β	Complete HT v_β	Final v_β	Initial $[V_\beta]$	Reach HT $[V_\beta]$	Complete HT $[V_\beta]$	Final $[V_\beta]$
WR-HT2	1113 (840)	0.043	0.25	0.18	0.047	0.208	0.072	0.088	0.175
PBF1-HT1	1043 (770)	0*	0.09	0.11	0.036	<i>NA</i>	0.104	0.106	0.206
PBF1-HT2	1113 (840)	0*	0.24	0.21	0.044	<i>NA</i>	0.070	0.081	0.206
PBF1-HT3	1281 (1008)	0*	1.0	1.0	0.060	<i>NA</i>	0.04	0.04	0.206

*To within our measurement resolution.

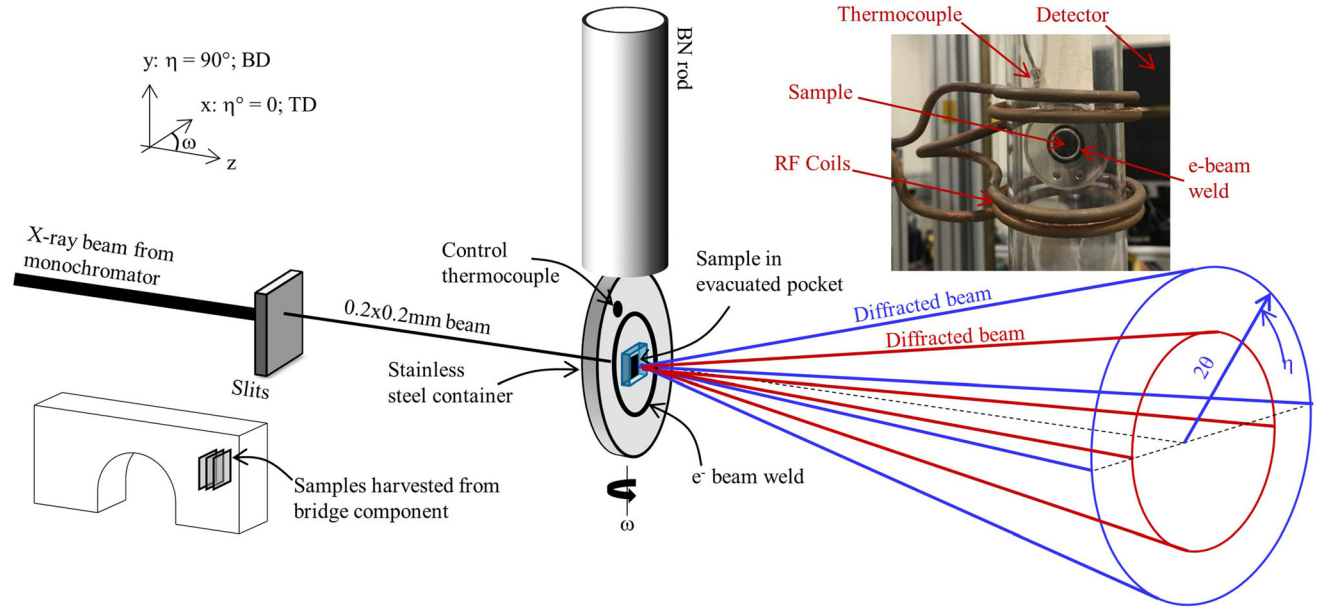


Fig. 1—Schematic and picture of the samples as harvested from the bridge component and experimental setup at the FAST beamline at CHESS.

in contact with the container roughly 10 mm from the sample position was used for real-time control of the container temperature. The 0.2×0.2 mm monochromated incident X-ray beam (69.525 keV, $\lambda = 0.17832$ Å) impinged normal to the steel container and Ti64 sample at $\omega = 0$ deg and was scattered onto a 2-dimensional GE 41RT detector with 2048×2048 pixels (0.200×0.200 mm pixel size).

The position of the detector changed depending on the specific microstructural quantity to be measured. First, the texture of each sample was measured with the detector centered on the transmitted X-ray beam located 811 mm downstream from the sample position. Twenty diffraction patterns were collected at equal intervals of ω from -50 to 50 deg for determination of the full Orientation Distribution Function (ODF). Next, the detector was moved on a motorized translation system further downstream from the sample to 1630 mm to improve resolution and offset laterally such that the transmitted beam was on the edge of the detector to increase the maximum 2θ to 16 deg, or an effective d -space range of 0.65 to 3.0 Å. These moves optimized the beamline characteristics for quantitative analysis of the diffraction line profile analysis (DLPA) to determine

dislocation content and character as well as average crystallite size of each sample. Finally, the detector was returned to position centered on the incident beam at an intermediate distance of 1086 mm downstream from the sample for the *in situ* heat treatment measurements. This position allowed for collection of full diffraction rings to a maximum 2θ of 10.4 deg, or an effective d -space range of 1 to 3.0 Å, encompassing 12 α -phase rings and five β -phase rings, sufficient for credible quantitative phase analysis. We maintain that measuring complete rings increases the accuracy of average d -space determination as it is more accurate to measure the diameter of the circle than to measure the radius. Texture measurements were repeated after the heat treatment. High-resolution line profile measurements were not repeated as the peaks were at or near the instrumental resolution making accurate line profile analysis impossible.

In situ heat treatments were completed at 1041 K (HT1), 1113 K (HT2), and 1281 K (HT3), just above the β transus, each with two-hour soaks at temperature. Table I shows a summary of sample nomenclature and conditions. By default, 2D diffraction images were collected with one second integration time every ten seconds throughout the thermal cycles. The temperature

was ramped at 100 K/min from room temperature until roughly 50 K below the target temperature, at which point the heating rate was reduced to 10 K/min to minimize overshoot of the target temperature. The thermocouple temperature was maintained at the target temperature via closed-loop control for nominally two hours. During cooling, the set point was reduced again at 100 K/min, but lacking an active cooling mechanism, the cooling rate decreased below ~700 K (~400 °C).

We note that a thermal gradient was anticipated between the sample and thermocouple position. Thus, while the real-time temperature control was achieved via the thermocouple, the reported sample temperature during the thermal cycle was determined from the evolving lattice parameter of the steel container and the known thermal expansion of 316L stainless steel [36] [37]. The roughly 30 microstrain uncertainty in the determination of the thermal strain of the steel coupled with the steel thermal expansion coefficient of $\sim 15 \times 10^{-6}/\text{K}$ results in an uncertainty in the temperature of roughly 2 K. A simple finite element model with the most conservative assumptions of heat transfer was used to estimate the maximum temperature difference between the sample and the container window near the sample. Due to the small mass of the sample, at the maximum heating rate of the container, the temperature difference between the sample and the container was less than 1 K. Thus, the temperature of the steel container determined from the diffraction data will be taken as the sample temperature at any given time. In fact, a temperature difference between the thermocouple and sample position of roughly 10 K was observed. Moreover, small drift of the temperature at the sample position relative to the controlled thermocouple temperature, again of roughly 10K, was observed during the soak time.

The ramp to the highest temperature, 1273 K, was paused briefly at ~873K to switch the detector from continuous imaging every 10 seconds to “burst mode” where 240 patterns, the maximum allowed by detector memory, were recorded at 0.67 Hz during the expected rapid microstructural evolution near the β transus. Diffraction measurements were not taken during the HT3 soak above the β transus because the large β grains produce intense diffraction peaks that threaten to damage the detector. Again, the detector was run in burst mode at the initiation of cooling to better capture the dynamics of the β to α transition, necessitating a ~five minute pause in cooling at ~900 K (~600 °C) while the 240 images were saved and the detector mode was returned to continuous imaging mode for the final cooling to room temperature. For baseline comparison, a wrought (hot rolled and annealed at 1255 K (982 °C)) Ti64 sample was taken through a heat and soak identical to PBF1-HT2, 1113K (WR-HT2).

While the experiments were performed and analysis completed on the AM sample made with the laser track at 45 deg relative to the sample axis (PBF2), the results from this sample were not significantly different from PBF1 and will not be discussed further.

D. X-ray Data Analysis

1. Texture analysis

The calibration of detector distance, orientation, and instrument parameters was completed with a CeO₂ powder standard. Synchrotron X-ray diffraction images were analyzed with the Rietveld method^[38] as implemented in the program package MAUD^[39] to determine the ODF. The analysis procedure was similar to Reference 40. For the texture analysis, the extended WIMV^[41] model was chosen.

2. Phase analysis

To monitor the evolution of the α and β phase concentrations, the 2D diffraction images were integrated over the full 360 deg range of η , the azimuthal angle about the incident X-ray beam, using GSASII^[42] to make a single 1D diffraction pattern from each image. Rietveld refinement of the binned 1D diffraction patterns was completed using an automated fitting routine (SMARTsware^[43]) to drive the original GSAS software^[44] to determine the phase fractions at each measurement point. Lattice parameter, phase fraction, peak breadth, and texture coefficients (8th-order spherical harmonics) of each phase, α - and β -Ti64 as well as face-centered cubic stainless steel, were allowed to vary during the refinement. For stability sake, the Debye-Waller factor was kept fixed during the refinements. Quoted uncertainties throughout are based on the estimated standard deviations (esd's) returned by GSAS.

The sample mounting fixture was not robust enough to ensure that the each sample was placed precisely (to better than ~0.5 mm) in the same position relative to the diffractometer center. Thus, the integrated (over η) room-temperature lattice parameter obtained from the steel container was used as an on-board calibrant to cross-calibrate the various samples against each other and enable direct comparison across multiple samples. In all cases, the correction factor so determined was less than 0.2 pct of the measured absolute lattice parameter.

3. Diffraction line profile analysis

Quantitative diffraction line profile analysis (DLPA) of the α phase in the as-built state was completed using the extended Convolutional Multiple Whole Profile (eCMWP)^[45,46] analysis software to obtain sub-grain sizes and dislocations densities with the assumption of dislocation of a type Burger's vectors. The methodology of the employed DLPA procedure has been discussed in detail in previous work.^[47] The area-weighted average coherent scattering domain size, X , and dislocation density, ρ , were determined with uncertainties of roughly ± 10 pct. The Wilkens dislocation arrangement parameter (M) fluctuated strongly because the shape of the tails was not captured well by the data so we chose to fix $M = 2.08$, a typical value for a cold-worked metal.

4. Lattice strain and peak breadth

Integration of the diffraction rings over the full range of η averages out any orientation-dependent effects (in the sample coordinates system) and artificially degrades the instrumental peak breadth. Moreover, Rietveld

refinement effectively averages over all crystallographic orientations,^[48,49] again smearing out interesting orientation-dependent effects. Thus, to monitor the evolution of the lattice spacing and peak breadth, each 2D diffraction image was binned into twenty-four 15 deg intervals in η using GSASII^[42] to make individual 1D diffraction patterns with diffraction vectors nearly (~ 4 deg off) transverse to the incident beam and in the plane of the sample. These 1D patterns have diffraction vectors that range from the build direction (BD), $\eta = 90$ and 270 deg, to the transverse direction (TD) $\eta = 0$ and 180 deg of the sample. Single-peak fits to determine the peak intensity, position in 2θ , and Gaussian breadth^[44] were completed on the α -100, 002, 101, 102, and 110 peaks as well as the β -110 and 200 peaks at each η for each run throughout the thermal cycle (roughly 150,000 single peak fits per sample) using an automated routine (APSSpf^[43]). The distinct responses of several peaks within a specific diffraction pattern with approximately co-linear diffraction vectors defined by the instrument geometry represent the average response of multiple distinct and mutually exclusive grain sets each with a specific plane normal aligned with the diffraction vector.

Fit 2θ values obtained from opposite sides of the diffraction rings, e.g., at 0 and 180 deg, are used to find the diameter of the rings and, subsequently, the inter-planar spacing normal to the specified (hkl) crystallographic plane, d_{hkl} , from Bragg's Law, $\lambda = 2d_{hkl}(\eta)\sin[\theta_{hkl}(\eta)]$. Where reported, lattice strains at temperature (T) and $\varepsilon^{hkl}(T,\eta)$ are calculated from $\varepsilon^{hkl}(T,\eta) = \frac{d^{hkl}(T,\eta) - d_0^{hkl}}{d_0^{hkl}}$, where d_0^{hkl} is taken to be the value determined at room temperature after the thermal cycle, as that is considered to be the best approximation to an equilibrium unstrained lattice spacing. The assumption of a specific d_0 value affects the absolute value of strain determined but minimally affects trends and/or crystallographic coefficients of thermal expansion (CTE's) determined from the slope of the data.

Data collected *in situ* during the heating was not sufficient for DLPA. However, information about the microstructure can be gleaned from the diffraction peak breadth. The diffraction peak is assumed to be Gaussian and the instrumental contribution to the peak width is subtracted in quadrature.^[44] The diffraction peak width is frequently assumed to be associated with dislocations and/or finite crystallite domain (sub-grain) size, although other microstructural effects can also increase the peak breadth. In this work, we will use the Full Width at Half Maximum (FWHM) as a qualitative indicator of the evolution of the dislocation density during the heat treatment to understand how the dislocation density decreases from the quantitative value found in the as-built state.

Due to the instrument specifics and geometry, the instrumental resolution is optimized (instrumental peak width is narrowest) at $\eta = 90$ and 270 deg, parallel to the build direction. Thus, the results shown in what follows will focus on this particular diffraction vector, but the results are consistent across all the observed diffraction vectors.

III. RESULTS

A. Material Characterization

EBSD orientations maps assuming an hcp (α) crystal structure of the wrought material before and after the heat treatment (HT2) are shown in Figures 2(a) and (b), respectively. β phase areas are represented by black. The initial α grain structure is equiaxed with average grain size of roughly 7 μm . After the heat treatment, the α grain structure appears to be bimodal, and the average size has increased to roughly 10 μm . The (110) texture has strengthened.

The as-built microstructure of the hcp phase in the PBF1 material is shown in Figure 3(a); those of the heat-treated materials in Figures 3(b) through (d). The build direction in the micrographs is out of the page. The initial grain structure of the PBF material is much finer than the wrought. While the current work provides no direct evidence of the martensitic transformation, similar microstructures built through the same process are commonly referred to as the α' phase^[50] indicative of a martensitic transformation mechanism. This morphology is commonly observed in additively manufactured Ti64 due to the rapid heating, melting, and solidification that occurs with each laser pass.^[16,18] The laths grow with increased heat treatment temperature. The inset in Figure 3(c) shows the average lath width as a function of the heat treatment temperature. The average lath spacing in the as-built material is slightly below 2 μm increasing with the heat treatment temperature to over 5 μm after the β phase soak.

EBSD identification of the crystal structure was unable to index any of the body-centered cubic (BCC) β phase in the as-built material. It is possible that the β phase is still present but not identified by the relatively coarse EBSD as β grains may be very small.^[18] In the heat-treated material, the β phase is indicated by black and is evident, in particular, following the highest temperature heat treatment at 1281 K and, to a lesser degree, the heat treatment to 1113 K.

Figures 4(a) and (b) show a limited section of the diffraction patterns collected on (a) laser powder bed fusion (PBF1) and wrought material (WR) material with the instrument in high-resolution mode and (b) PBF1 is the as-built condition and after the two-hour soak at 1043 K (PBF1-HT1) with the instrument in *in situ* mode that is with lower resolution. The peaks are indexed according to the α and β phases. A powder diffraction measurement cannot distinguish between α and α' other than a relatively small change in the lattice parameters between the two microstructures^[7,13] and the HCP phase will simply be referred to as α from here on. The diffraction peaks from the as-built PBF1 material are significantly broader than their counterparts either in the WR or heat-treated PBF1 material. Also, the lack of the β -110 peak is apparent in the as-received material; the material is pure α to within our resolution in this condition, although β volume fractions less than 0.01 with very small grains (*i.e.*, very broad peaks) could go undetected. Finally, despite subtle on this scale, it is apparent that the α peaks from the as-built PBF1

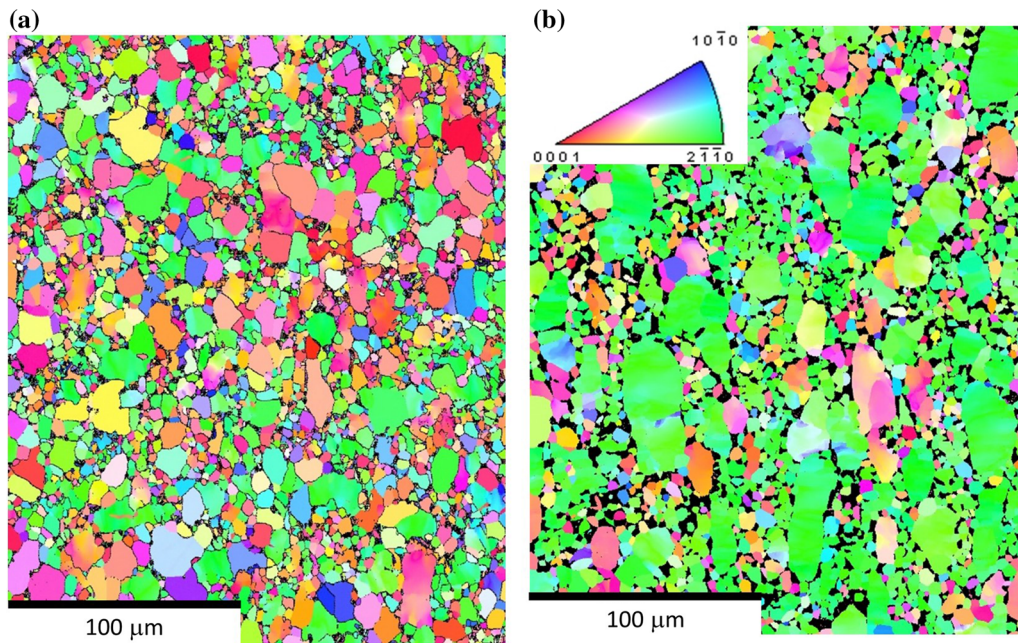


Fig. 2—EBSD maps of the wrought material (a) before and (b) after HT2. The rolling normal direction is out of the page.

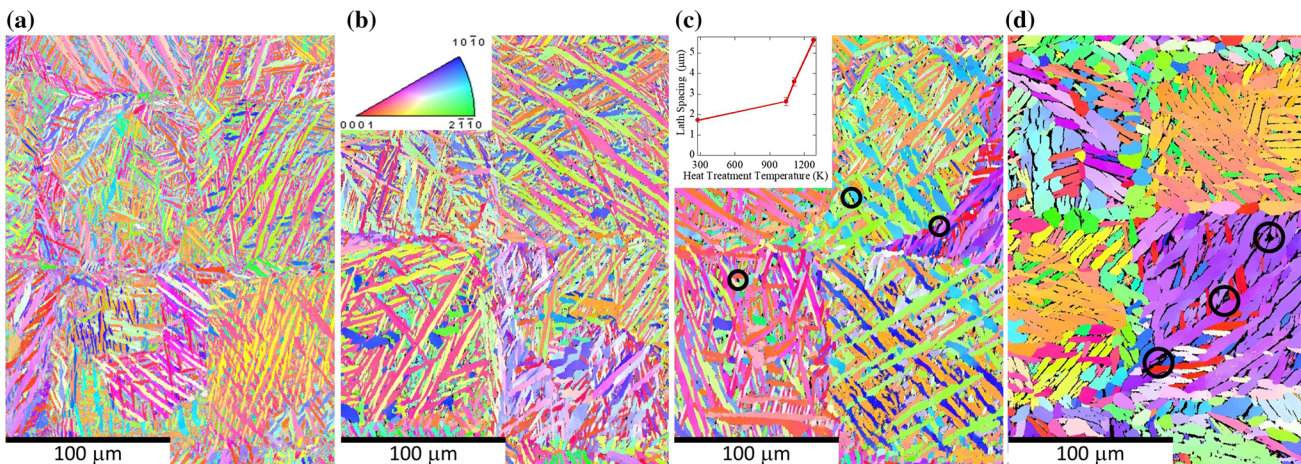


Fig. 3—EBSD maps of the PBF1 material in the (a) as-built condition as well as after heat treatments of (b) 1043 K (770 °C), (c) 1113 K (840 °C), and (d) 1281 K (1008 °C). The build direction is out of the page. The inset shows the lath spacing as a function of the heat treatment temperature. Black areas are β phase indicated by black circles.

material are at slightly lower d-spacing than either the WR or heat-treated PBF1 material.

Figures 5(a) through (d) show the α -(100), (002), and (110) pole figures representing projections of the ODF of the (a) as-received and (b) heat-treated wrought (WR-HT2) materials as well as the (c) as-built and (b) heat-treated powder bed (PBF1-HT2) materials. The initial texture of the wrought material is moderately strong as expected for rolled material and strengthens slightly following the thermal cycle to 1113 K. The PBF material has a relatively weak texture in the as-built condition and is almost completely random following the thermal cycle to 1113 K. While not shown for brevity, the as-built and post-heat treatment textures of the PBF material heat treated to 1043 K

and 1273 K were not significantly different from that shown.

B. *In Situ* Heat treatment

Figure 6 shows the observed thermal profiles for each of the heat treatments presented herein. As is the case in most of the plots shown below, only every tenth collected data point is shown. While the set temperature and thermocouple temperature were held fixed throughout the two-hour soak, the temperature of the sample did evolve slowly. For example, while the target temperature was 1043 K (770 °C), PBF1-HT1 warmed slowly from 1038 K to 1047 K during the two-hour soak. Likewise, the PBF1-HT2 sample cooled from 1118

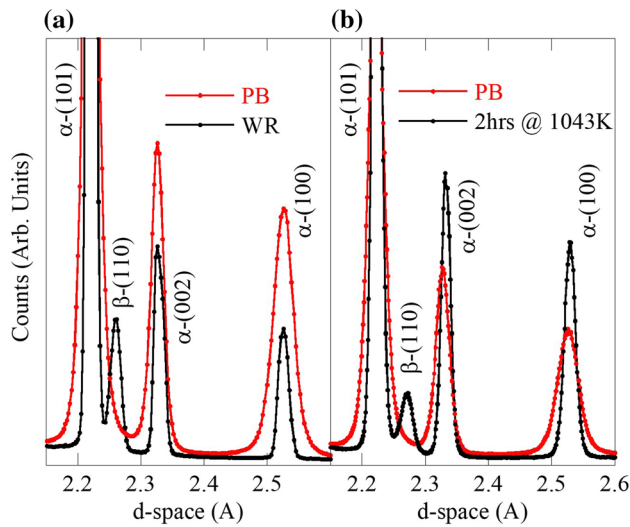


Fig. 4—Sections of diffraction pattern collected on (a) powder bed (PB) and wrought (WR) Ti64 in high-resolution mode and (b) powder bed material in the as-built (AB) condition and after the two-hour soak at 1043 K in medium resolution mode. The peaks are indexed according to the α and β phases.

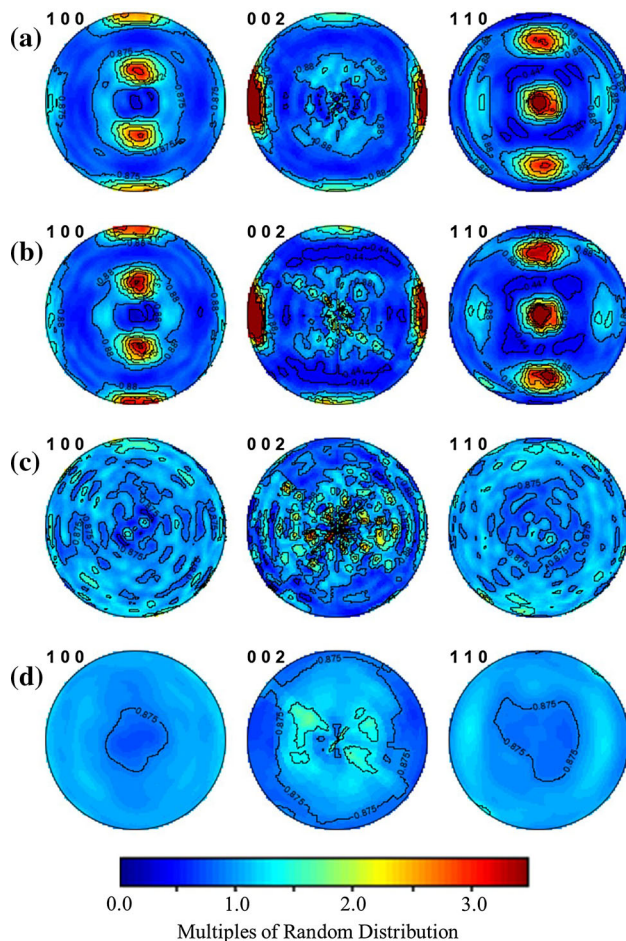


Fig. 5—Pole figures representing the texture of the wrought material (a) as-received and (b) following HT2 and the PBF1 material (c) as-built and (d) following HT2. For the wrought material, the rolling normal direction is out of the page. For the PBF1 material, the build direction is out of the page.

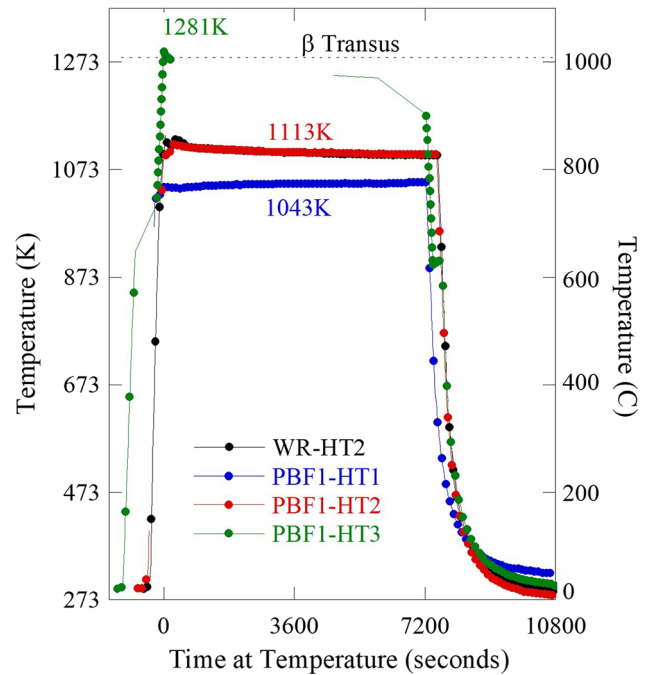


Fig. 6—Observe thermal profiles for the samples heat treated as part of this work.

K to 1102 K during the soak. As a reminder, data were not collected during the soak of HT3 because of the risk to the detector from large β grains, so the exact soak temperature and its evolution are not known. The wrought sample underwent HT2 although it is difficult to see in the plot as it is essentially covered by PBF1-HT2 data. The specified heating rate of each sample was 100 K/min. The realized heating rate determined from the data shown in Figure 6 was observed to be very close to this in all cases.

The *in situ* diffraction measurements enable monitoring of the microstructure from the as-built state to the post-heat-treated state. The most obvious microstructural evolution during heat treatment is the evolution of the phase from essentially single phase α to, eventually, the stable two-phase $\alpha + \beta$ microstructure following the thermal cycle. Figures 7(a) and (b) shows the evolution of the β volume fraction, v_β , in the wrought and powder bed materials as a function of (a) time and (b) temperature, respectively, throughout the various heat treatments. The estimated uncertainty in the β volume fraction of 0.004 is indicated. In Figure 7(b), the data collected on cooling are shown as open symbols and dotted lines to aid in distinction from the data on heating. The inset to Figure 7(b) highlights the region to $v_\beta = 0.30$. Table II lists v_β at various stages for each of the samples studied.

The wrought material had an initial β phase fraction consistent with expectations for a wrought Ti64 plate. At ~ 900 K (~ 727 °C), v_β begins to increase in the wrought alloy at an appreciable rate to the soak temperature of 1113 K. The β -phase content decreases slowly during the two-hour soak. Recall that the observed temperature of the sample container in contact

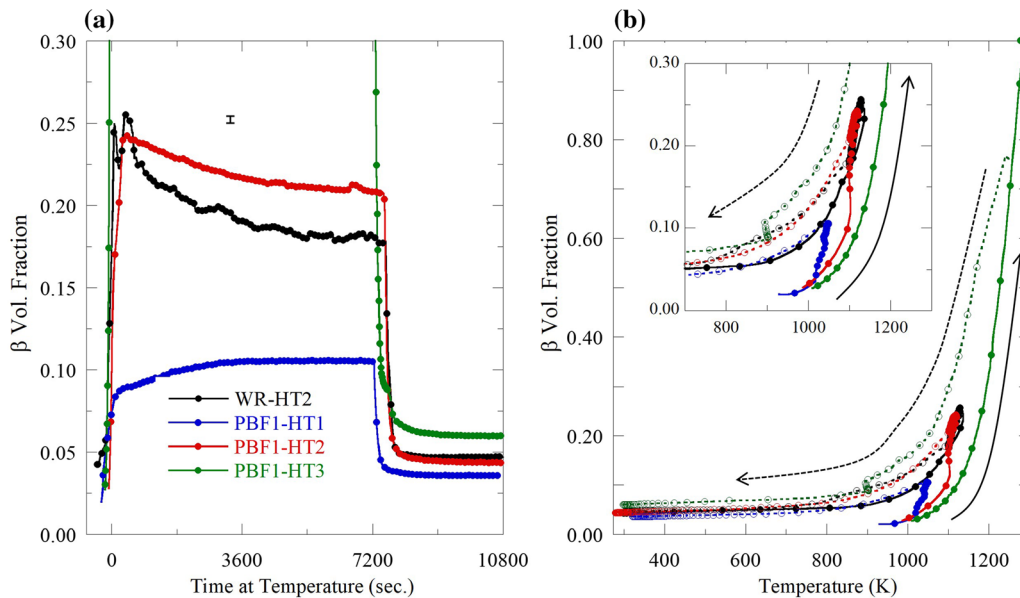


Fig. 7—Evolution of the β volume fraction in the wrought (WR) and powder bed (PB) material with (a) time and (b) temperature during distinct heat treatments. The estimated uncertainty is indicated in (a).

with the sample reduced slightly from 1118 K to 1102 K over this same time. Upon cooling, v_{β} decreases to slightly higher than the initial β phase fraction.

No β phase is present in the powder bed material initially. The first evidence of the β -110 peak, the strongest β phase peak, in the diffraction patterns from the powder bed material appears between 913 K (640 °C) and 923 K (650 °C) during heating but is not quantifiable until it reaches a volume fraction of ~ 0.02 at roughly 950 K (677 °C). When PBF1 reaches the nominal 1043 K soak, v_{β} is 0.09 but continues to slowly increase over the first hour of the soak to 0.11. The β fraction in PBF1-HT2 nearly matches that achieved by WR-HT2, and, similar to the wrought material, slowly decreases during the soak. However, the β fraction in the powder bed material decreased less to 0.21 at the end of the soak, compared to the wrought material. PBF1-HT3, heated above the β transus, achieved complete transformation to the β phase.

The time-dependent changes in the β fraction during the nominally isothermal holds are difficult to interpret because of the small evolution of temperature witnessed. Elmer *et al.*^[51] report the equilibrium change of β fraction with temperature at 1043 K (779 °C) and 1113 K (840 °C) as 0.0012 mole fraction/K and 0.0029 mole fraction/K, respectively. While isothermal evolution of the β fraction during the hold cannot be eliminated, the observed changes in β fraction during the holds are correct in sense and roughly consistent in magnitude with the observed temperature change of + 9 K during HT1 and - 16 K during HT2.

During cooling from the soak temperature, at any given temperature, v_{β} is greater in the samples heated to higher soak temperature, i.e., the β volume fraction is a function of the full soak history. Upon reaching room temperature, the final β fraction is a monotonic function of the maximum temperature reached during the heat

treatment. Having gone to the same soak temperature, PBF1-HT2 and WR-HT2 return to room temperature with the same β volume fraction within the specified uncertainty. The temperature hold for roughly five minutes during of PBF1-HT3 at ~ 900 K (~ 600 °C) while the detector was reset is interesting because of the continuous decrease in v_{β} from 0.11 to 0.09 during the pause in cooling. Clearly, the material is not in equilibrium while cooling at 100 K/min.

During heating, the first significant observation in the evolving diffraction pattern, prior to the inception of the phase transformation, is the reduction of the diffraction peak breadth. Figure 8(a) shows the evolution of the FWHM ($\Delta d/d$) determined in several single peaks in the diffraction pattern with diffraction vector parallel to the build direction during heating and subsequent cooling of the powder bed material. The differences of peak width in the as-built condition are dependent on crystallographic orientation as opposed to d-spacing. The 002 and other near basal peaks exhibit the least broadening while the 110 peak is the broadest, suggesting *a* type dislocations according to the dislocation contrast factors.^[52] Quantitative diffraction line profile analysis of the PBF1 material yielded an average coherent scattering domain size (sub-grain size) of $X = 23 \pm 3$ nm and dislocation density $\rho = (4 \pm 0.5) \times 10^{15}/\text{m}^2$.

Little evolution of the FWHM in any of the grain orientations is observed until 770 K (497 °C) when the width begins to decrease precipitously and simultaneously in all observed grain orientations signaling the onset of recovery. Note, the reduction of the peak width prefaces the initiation of the transformation to the β phase by roughly 150 K. The peak widths have decreased by roughly 75 pct by 950 K when the β phase first becomes significant. The width has not reached its minimum value at the HT1 soak temperature of 1043 K but continues to decrease with time at nominally

Table II. Observed CTE of Distinct Grain Orientations in the α and β Phases in the Wrought and Powder Bed Material on the Various Heating and Cooling Cycles

Orientation	Wrought		PBF	
	H ($\times 10^{-6}/\text{K}$)	C ($\times 10^{-6}/\text{K}$)	H ($\times 10^{-6}/\text{K}$)	C ($\times 10^{-6}/\text{K}$)
α -(100)	10.2	9.4	9.4	10.9
α -(110)	9.9	9.6	9.3	11.1
α -(101)	9.9	9.8	10.2	11.3
α -(102)	9.9	9.7	9.5	11.2
α -(002)	9.7	10.0	10.1	11.4
β	8.8	9.3		9.5

Uncertainty in the α phase is ± 0.2 , in the β phase is 0.5.

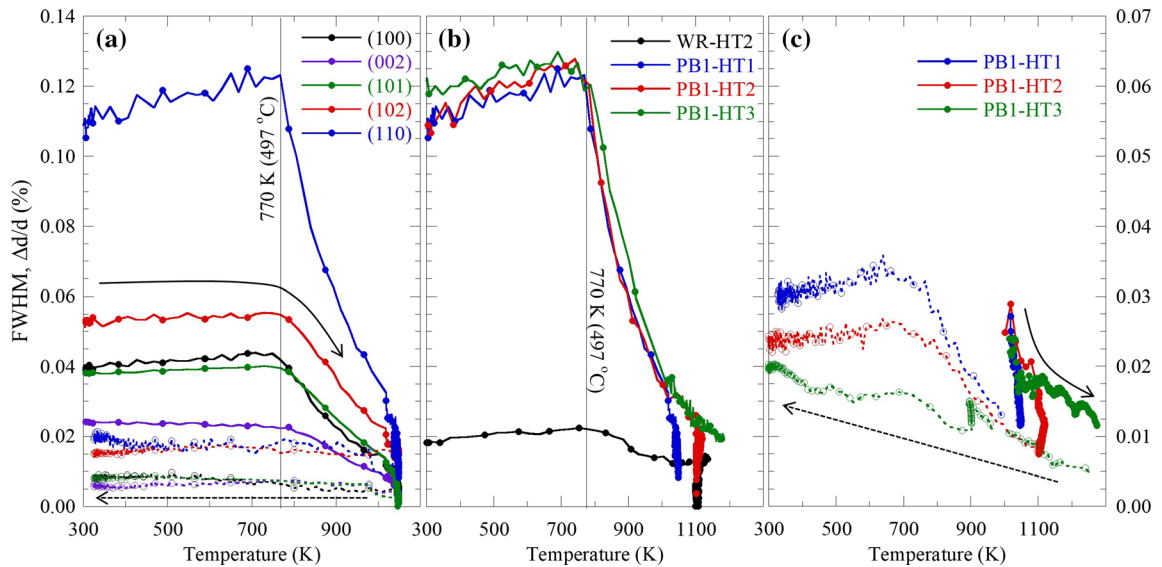


Fig. 8—(a) Evolution of the peak widths (FWHM) of several single peaks (hkl) in the PBI-HT1 material during heat treatment. Evolution of the (b) a-(110) and (c) b-(110) peak variances in the wrought (WR) and powder bed material (PBF) during the distinct heat treatments. Closed (open) symbols represent data taken on heating (cooling). Cooling data are not shown in (b).

constant temperature before remaining constant during cooling. No attempt was made to obtain dislocation density in the annealed material as the peak widths were very near the instrumental resolution.

Figure 8(b) shows the evolution of the α -110 peak, the broadest peak, during the heat treatment of the wrought material (WR-HT2) and all three heat treatment temperatures. Data collected during cooling are not shown. The 110 peak width from the wrought material is initially an order of magnitude lower than that of the powder bed material and remains constant until nearly 900 K above which it decreases slightly. While data were collected for quantitative analysis of the dislocation density, the peak breadth from the wrought material was too near the instrumental resolution for accurate parameter determination. The repeatability of the measurements over the three displayed heat treatments (and fourth, PBF2, not shown) of the powder bed material is remarkable. During the higher temperature heat treatments, the 110 peak width continues to decrease with increasing temperature. At 1113 K, the width has still not reached its minimum value and, again, continues to decrease isothermally with time at temperature. Just

beyond 1173 K (900 °C), on the way to HT3, the α peak intensities have decreased such that the peak widths can no longer be determined with sufficient accuracy.

Figure 8(c) shows the evolution of the width of the β -110 peak, the only β peak strong enough to obtain an accurate width before the peak width decreases to within uncertainty of the instrumental resolution. Note that the scale is reduced from that in Figures 8(a) and (b) by a factor of 2. When the β -110 peak first appears, the width is roughly 0.03 pct and quickly decreases as the temperature increases. The agreement between the three cases is again remarkable. On cooling, the behavior of the β -110 peak width is distinct from the α peaks, increasing with decreasing temperature until, apparently, saturating. Interestingly, the final width of the β -phase peak is dependent on the maximum heat treatment temperature: the higher the heat treatment temperature, the lower the width when room temperature is achieved. PBF1-HT3 is again distinct because of the short pause during cooling to refresh the detector. The peak breadth decreases during the hold at 900 K but increases again when cooling to room temperature continues. The available peak breadth data from the β phase, from a single grain

orientation, are insufficient for interpretation in terms of microstructural features.

Figures 9(a) through (f) shows the evolution of the interplanar (d -) spacings of the α -phase 100 and 102 peaks at distinct angles about the incident beam (η) with temperature during heating and cooling. Figures 9(a) and (d) shows the heating cycle of the wrought material to 1113K (WR-HT2). The cooling cycle is not shown because it overlaps with the results on heating. Figures 9(b) and (e) show the powder bed material to 1043 K (PBF1-HT1) and (c) and (f) 1281 K (PBF1-HT3). Recall that $\eta = 90$ and 0 deg probe the build and transverse directions of the sample, respectively. The α (100) and (102) are shown because they have the best signal-to-noise at all values of η and are well separated from any β phase peaks, but the results are general to all five α peaks analyzed. The relative uncertainty in the determination of the d -spacings of the (100) and (102) varies with η as the texture affects the peak intensity but is roughly ± 0.0001 Å and ± 0.00007 Å, respectively. The wrought material behaves as expected. The interplanar spacings are independent of η , and the thermal expansion is nearly linear with heating, the slope increasing slightly with increased

temperature. There is no hysteresis observed between heating and cooling of the wrought material.

In the as-built state of the PBF1 material, there is a large variation in the α (100) and (102) interplanar spacing with orientation, η , which will be discussed further shortly. Also, when averaged over all orientations, the initial interplanar spacings of all of the peaks from the PBF1 material are significantly smaller than that of the wrought material. With heating, the interplanar spacings increase with roughly the same slope regardless of orientation until 770 K (493 °C). At this temperature, the apparent thermal expansion becomes significantly non-linear and η dependent; the variation of the interplanar spacings with orientation begins to collapse. By 873 K (600 °C), before a significant amount of the β phase has appeared, that variation has reduced to below the level of the uncertainty. With continued increasing temperature, the d -spacing continues to increase with increasing temperature equally for all values of η . During the hold at 1043 K, the interplanar spacing increases, more than can be attributed to the slight increase in temperature (9 K) observed during the hold. With heating directly to 1281K, the interplanar

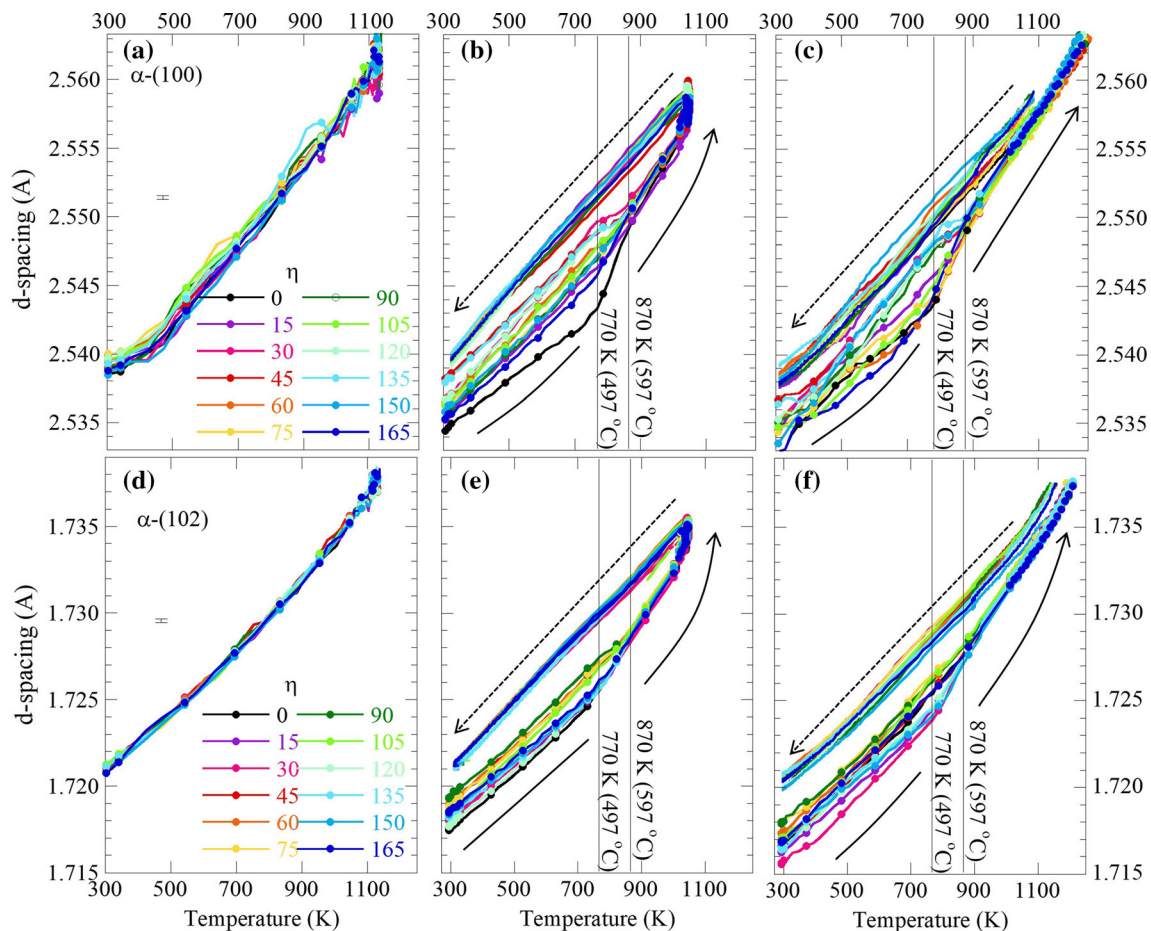


Fig. 9—Evolution of the interplanar (d -) spacing of the (a) through (c) (100) and (d) through (f) (102) planes along different sample directions (η) during heat treatment and subsequent cooling in the (a) and (d) wrought material (b) and (e) PBF1-HT1 and (c) and (f) PBF1-HT3. Only heating is shown in the wrought material. The arrows indicate the direction in the PB materials. No symbols are shown on cooling as they overlap considerably. Representative uncertainties are shown in (a) and (d).

spacings continue to increase independent of orientation beyond 873 K until the α phase disappears.

In contrast to heating, with cooling, the α (100) and (102) interplanar spacings decrease nearly linearly with no significant orientation dependence. As room temperature is approached on cooling, the d-spacing of each peak is orientation independent to within measurement uncertainty and is within uncertainty of the wrought material d-spacing, significantly higher than the interplanar spacings in the as-built condition.

The described evolution of the lattice spacing is general for the α -(100), (002), (101), (102), and (110) plane normals. The one difference between the different plane normals is the variation of the interplanar spacing with respect to the orientation, η , in the as-built condition. Figures 10(a) through (e) shows the fractional variation of the interplanar spacings (strains) as a function of η for the five α peaks in the powder bed material in the as-received condition (blue) and after the heating cycles to 1043 K and 1281 K (red). The orientation averaged interplanar spacing after the final heating cycle is taken as the reference for calculation of the strain.

In the as-built condition, the variation of the interplanar spacings with orientation is systematic and large. For example, the α -(100) interplanar spacing is smallest near the TD ($\eta = 0$ deg) and BD ($\eta = 90$ deg) and largest at $\eta = 45$ deg. In contrast, while the statistical uncertainty in the determination of the α -(002) d-spacing is significantly larger than the other orientations, there is little variation of the α -(002) interplanar spacing with η in the as-built powder bed material. Moreover, while orientation dependence of the interplanar spacing is evident in the α -(102) and α -(110) grain orientations, the dependence is distinct from the α -(100). Specifically, where the α -(100) d-space is a minimum $\eta = 0$ and 90 deg, the α -(102) is a minimum at 30 and 120 deg.

It has been previously argued that the observed lattice strains in the as-built PBF1 material must be due to intergranular residual stresses that develop due to plastic deformation driven by the extreme thermal gradient during cooling from solidification.^[53] Note, the

variation with η is not precisely the same for the PBF1-HT1 and PBF1-HT3, which is also apparent in Figures 10(b) and (c). The differences are small but may represent local variations within the original build; the samples were cut side by side. The general behavior is consistent, however.

The orientation dependence of the interplanar spacings associated with intergranular residual stresses evident at room temperature disappears in all cases over the same temperature range, between 770 K and 870 K as shown for the α -(102) in Figure 9(b). With return to room temperature after the thermal cycle, the observed variation of the interplanar spacing is within uncertainty of zero at all orientations. Figure 9 also clearly demonstrates how the orientation averaged d-spacing increases in all cases following the heat treatment of the powder bed material.

Figures 11(a) through (c) shows the analogous thermal response of the β -110 peak in (1) the wrought material. (b) HT1 and (c) HT3 of the PBF1 material. Note the scale of Figure 11 is larger ($\times 2$) than that of Figure 9. Initially, the β -(110) interplanar spacing in the wrought material increases linearly until roughly 820 K (547 °C) where the slope decreases slightly before increasing significantly above 900 K (627 °C) until the end of the temperature range. The arrest between 820 K and 900 K is consistent with reported observations^[13] where it is associated with vanadium partitioning between the α and β phase during heating of wrought Ti64. There is significant hysteresis on cooling. The initial slope during cooling is significantly less than that as the maximum temperature was reached during heating. From 650 K to room temperature, the slope on cooling is similar to that on heating. The β (110) interplanar spacing at room temperature is larger in the wrought material following the thermal cycle than it was in the as-received condition. The wrought material was received in a hot-rolled and annealed condition; the final step was a near β anneal followed by air (slow) cool. Thus, the wrought material was presumably in the equilibrium condition as received, prior to the thermal

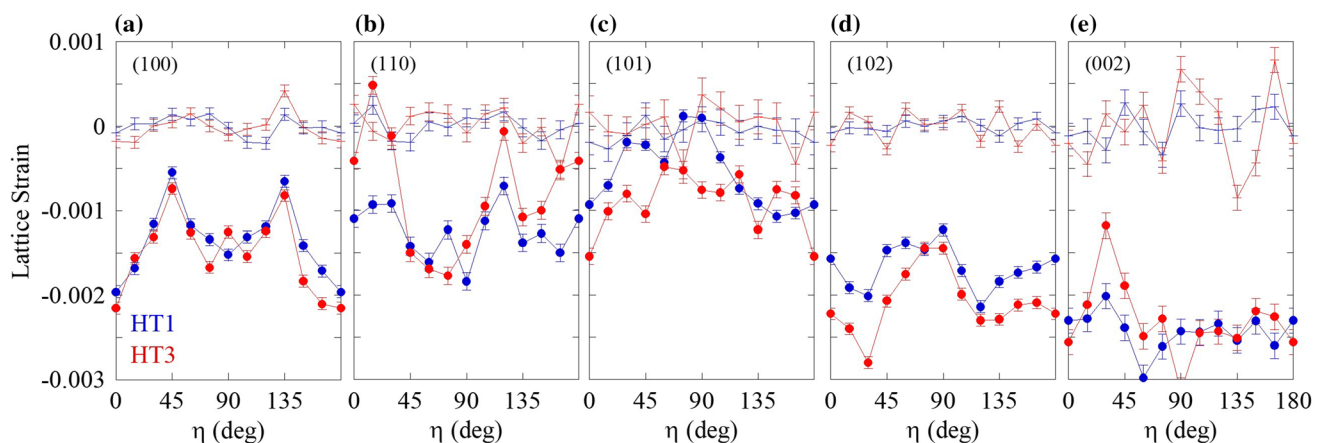


Fig. 10—(a) through (e). Lattice strain for several plane normals as a function of orientation about the sample normal. Red and blue data represent strains from the PBF1-HT1 and PBF1-HT3 sample before (filled circles) and after (+) the heat treatment (Color figure online).

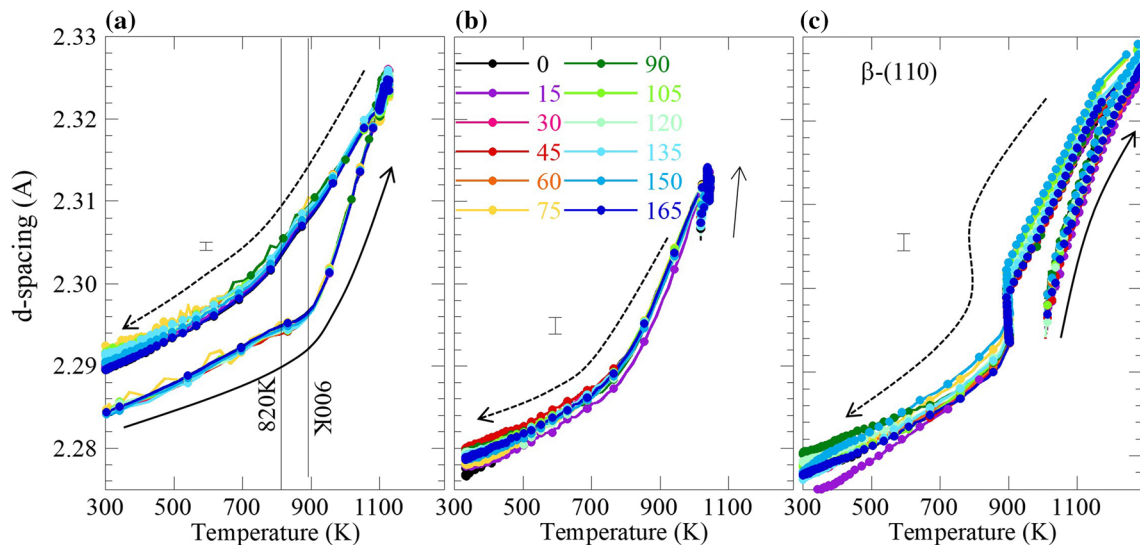


Fig. 11—Evolution of the interplanar (d -) spacings of the β (110) along different sample directions (η) during heat treatment and subsequent cooling in the (a) wrought material, (b) PBF1-HT1, and (c) PBF1-HT3. Representative uncertainties are indicated.

cycle and relatively fast cooling (100 K/min) experienced in this study.

Figures 11(b) and (c) shows comparable data from the PBF1-HT1 and HT3 samples. Of course, no β phase is present at the start of the heating cycles. When the temperature reaches 1018 K (745 °C), the diffraction signal from the β phase is first strong enough to enable determination of the interplanar spacing with sufficient accuracy. The β phase appears at roughly the same temperature during HT3 as HT1, but the lattice parameter is smaller in HT3 than HT1. We do not have an obvious explanation for this small difference between the β phase lattice parameter in HT1 and HT3. Sample HT3 experienced a slightly different heating trajectory being held at \sim 900K for 5 minutes to switch detector configuration. At this stage of heating, the only changes in the microstructure observed in the diffraction data are the reduction of peak width and the intergranular residual stresses which happen concurrently above 770K. However, both of these effects are consistent between HT1 and HT3, *i.e.*, are not affected by the distinct thermal trajectory of HT3. Moreover, the intermediate hold temperature of HT3 is below the appearance of the β phase.

The β (110) d -spacing increases sharply to the soak temperature of 1043K and continues to increase isothermally. With cooling, the interplanar spacing again decreases relatively quickly until roughly 800 K, where the slope decreases significantly. Time-dependent isothermal contraction of the β (110) is observed during the hold at 900 K when cooling from HT3. At room temperature, the β (110) interplanar spacings in the heat-treated powder bed materials are still significantly less than the wrought material. The β -200 peak was also analyzed but with significantly worse uncertainties and provides no distinct insight.

IV. DISCUSSION

The Ti64 material manufactured with laser powder bed fusion has a high-energy, metastable microstructure in the as-built condition. The material is locked in this condition by the high cooling rates experienced during the build. This provides an opportunity to control the final microstructure, and thus properties, of the material through an informed heat treatment process. The experiments described herein were carried out with this in mind.

The microstructural state clearly evolves during heating from the as-built state. The lattice parameter and/or interplanar spacings are very sensitive to changes in the microstructure and are measured with a high degree of accuracy so can be utilized to track the evolution. The dominant effect on the interplanar spacings during a thermal cycle is simple thermal expansion,^[31] which can change the lattice parameter by rough 1 pct over an 800 K temperature change. While thermal expansion is often slightly non-linear, the highly non-linear expansion of the lattice of both phases during heating from the as-built condition is not attributable to simple thermal expansion but rather must be related to other changes in the microstructure. To observe the effect of more subtle microstructural changes, *e.g.*, solute chemistry or internal stresses, on the d -spacings, it is advantageous to remove the thermal expansion from the observations.

Effective CTEs were determined during heating and cooling along the different crystal plane normals in the α and β phases of both the wrought and PBF material. As the lattice expansion was distinctly non-linear during heating above 700 K, the CTEs were determined by a linear fit to data between 373 K (100 °C) and 673 K (400 °C) for consistency. The results were averaged over all orientations η .

Table II lists the observed CTE's along specific α phase plane normals in the wrought and PBF material. For comparison, the bulk-averaged CTE of polycrystalline Ti64 is reported as $9.0 \times 10^{-6}/\text{K}$ at room temperature^[12,36] and $11.2 \times 10^{-6}/\text{K}$ at 700 K^[36], or $10.0 \times 10^{-6}/\text{K}$ ^[36] when averaged over the appropriate temperature range for direct comparison to the values determined herein. A small amount of crystallographic orientation dependence is reported in the CTE of Ti64 with that along the *c*-axis being slightly larger than along the *a*-axis.^[54]

The observed CTE in the wrought material is $(9.8 \pm 0.2) \times 10^{-6}/\text{K}$ in agreement with published results,^[36] and the variation of the observed CTEs with crystallographic orientation is near the level of the uncertainty. Likewise, the difference between heating and cooling of the wrought material is on the level of the uncertainty. During heating of the PBF material from the as-built condition, the CTE exhibits significantly more variation with crystallographic orientation relative to the average of $(9.7 \pm 0.2) \times 10^{-6}/\text{K}$. In contrast, on cooling, the orientation dependence of the CTE is once again at or near the level of the uncertainty. However, the observed orientation averaged CTE on cooling of $11.2 \times 10^{-6}/\text{K}$ is somewhat greater than on heating and greater than the wrought material.

The effective CTE of the β phase was determined in an analogous manner, except the lattice parameter of the β phase was used rather than single crystallographic orientations. The cubic phase cannot exhibit anisotropy of the thermal expansion, and significantly more precise results are gleaned from the lattice parameter of the minor phase compared to the strongest β peak. The observed β phase CTE in the wrought material is $8.8 \times 10^{-6}/\text{K}$ and $9.3 \times 10^{-6}/\text{K}$ on heating and cooling, respectively, within uncertainty of each other. Of course, the β phase CTE in the PBF material can only be determined during cooling and is $9.5 \times 10^{-6}/\text{K}$. For comparison, the reported CTE of β phase Ti alloy (Ti5553) averaged over the same range is $9.3 \times 10^{-6}/\text{K}$.^[36]

The lattice strain attributable to thermal expansion ($\alpha_{\text{CTE}}\Delta T$) can then be removed from the total observed lattice strain, $\epsilon_{\text{non-TE}} = \epsilon_{\text{obs}} - \alpha_{\text{CTE}} \Delta T$, to emphasize the changes due to phenomenon other than thermal expansion ($\epsilon_{\text{non-TE}}$) such as mechanical and chemical strains. The microstructure is expected to be more stable during cooling so the interplanar spacings and CTEs determined during cooling are considered to be the equilibrium values.

Figure 12(a) shows the non-thermal expansion (non-TE) strains for the α (102) during HT1 and HT3; the two results are offset from each other for clarity. Each crystal orientation (hkl) analyzed showed analogous behavior. It was noted earlier that there were slight differences between the initial distribution of lattice strains between HT1 and HT3, but the general response is the same. A similar plot for the β phase is shown in Figure 12(b) but is averaged over all η .

The α phase non-TE strains start offset from zero by an amount that is dependent on the orientation, η , relative to the samples axes, but averages to a strain of

-0.015. The orientation-dependent variation of the strain must be associated with residual stresses as chemical strains would be isotropic. Moreover, those residual stresses must be intergranular in nature as they are dependent on crystallographic direction.^[53]

The slow decrease of $\epsilon_{\text{non-TE}}$ with increasing temperature to 700 K is due to the observed difference in CTE on heating and cooling. Several microstructural changes occurred between heating and cooling including the texture, grain size, phase fractions, and vanadium concentration that could affect the observed CTE. The effect on the CTE is modest, and no attempt to separate these effects will be made herein. The orientation dependence collapses suddenly from 770 K to 870 K, signaling relaxation of the intergranular stresses that developed during deposition. The non-TE strain increases monotonically and independent of crystal orientation above 870 K until the β transus temperature in HT3. In HT1, $\epsilon_{\text{non-TE}}$ increases isothermally during the 2 hour soak. The non-TE strains are then close to zero during cooling. Little or no isothermal evolution of $\epsilon_{\text{non-TE}}$ is observed in the α phase at 900 K during the hold in cooling from HT3.

The non-TE strains in the β phase are roughly an order of magnitude larger than in the α phase. When the β phase first appears, they are somewhat positive and increase rapidly with temperature. Similar to the α phase, $\epsilon_{\text{non-TE}}$ increases isothermally in the β phase during the soak at 1043 K, HT1. During cooling, they decrease quickly to roughly 700 K. In contrast to the α phase, $\epsilon_{\text{non-TE}}$ decreases isothermally during the hold in cooling from HT3. From 700 K to room temperature, the non-TE strains in the β phase are essentially zero.

In the β phase, in particular, the non-TE strains are due to changes in solute chemistry during the phase evolution. The strains are very large, greater than 1 pct, and they occur concurrent with the transformation. The lattice parameter of the β phase in particular is sensitive to the amount of dissolved vanadium.^[55] In equilibrium, the vanadium concentration in the β phase goes from 4 pct at the transus, to nearly 100 pct at room temperature, while it only changes from near zero to a maximum of less than 5 pct in the α .^[51] Likewise, the change in aluminum concentration in the β phase is also relatively small, from 6 pct at the transus to nearly zero at room temperature.^[51] Moreover, the metallic radius of titanium (147 pm) is very different from that of vanadium (135 pm), much more so than that of aluminum (143 pm).^[51,56] Thus, the effect of aluminum on the lattice parameter of the β phase will be ignored in the following.

The lattice parameter of β Ti-V over the range of 20 at. pct to 50 at. pct (21 to 52 wt pct) vanadium is linear in vanadium concentration.^[55] By adding the lattice parameter of pure vanadium,^[57] a linear relationship between the lattice parameter and vanadium concentration of the form $a([V]) = 3.278\text{\AA} - 0.24[V]_{\beta}$ can be established for the Ti/V system over the entire range, where $[V]_{\beta}$ is the vanadium concentration in wt pct. The vanadium concentration in the β phase can then be written in terms of the strain due to solute chemistry as

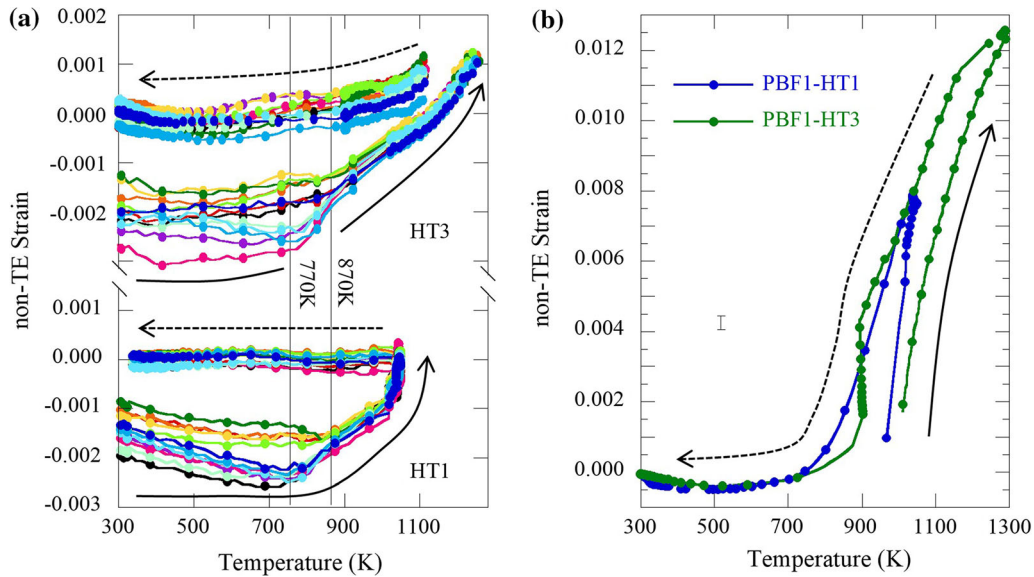


Fig. 12—Non-CTE strains in the (a) α phase along different sample directions (η) as in Figs. 9 and 11 and (b) the β phase (integrated over η) of PBF1 as a function of temperature during HT1 and HT3.

$[V]_{\beta} = -13.6\epsilon_{\text{Chem}}$. We assume that this form holds at least approximately for the TiAlV system except our measurement of zero strain comes at room temperature on cooling, when $[V]_{\beta} \neq 0$. Thus, there must be an offset which is determined by forcing the vanadium concentration to be 0.04 weight percent at the transus temperature, *i.e.*, when the material is fully in the β phase. With this constraint, the equation becomes $[V]_{\beta} = 0.208 - 13.6\epsilon_{\text{Chem}}$. The vanadium concentration in the α phase is then just the balance of the 4 wt pct. Using the results from Reference 55 as a calibration of the vanadium concentration is, at best, an estimate of the absolute concentration. However, the relative accuracy, in other words, the accuracy in the observed changes in the vanadium concentration with temperature and between PBF samples, should be roughly

proportional to the uncertainty in the strain measurement or roughly ± 0.003 (0.3 pct).

Figures 13(a) and (b) shows the vanadium concentration in the α and β phases in the (a) wrought and (b) PBF material as a function of temperature during the heating and cooling cycles. The values at several stages of the heat treatment are tabulated in Table II. Initially, $[V]_{\alpha}$ and $[V]_{\beta}$ in the wrought material are 0.032 and 0.208, respectively. This can be compared to $[V]_{\alpha}$ and $[V]_{\beta}$ of 0.014 and 0.154, respectively, determined by microprobe analysis in similar air cooled (from 998 K) material with a reportedly higher β phase fraction of 0.12^[51] and $[V]_{\alpha}$ and $[V]_{\beta}$ of 0.018 and 0.12, respectively, in forged material.^[14] As the wrought material had originally underwent a slow, “air cool,” process, we assume that the initial vanadium concentration is close to equilibrium.

The vanadium concentration in the β phase in the wrought material is stable until above 900 K (623 °C) when the $[V]_{\beta}$ drops rapidly as the total amount of β phase increases from the initial fraction of 0.043 to 0.24 at the maximum temperature of 1113 K (840 °C). During the soak, $[V]_{\beta}$ increased as the temperature slowly decreased. The vanadium concentration in the β phase is hysteretic during cooling, being significantly lower at any given temperature than it was on heating. Apparently, when cooling the wrought material at 100 K/min, the β to α transformation outpaces the vanadium diffusion, leaving some metastable vanadium trapped in the α phase. At room temperature, the vanadium concentration in the β phase of the wrought material is 0.175, significantly lower than prior to the thermal cycle. As the amount of α phase is $\sim \times 15$ larger than the amount of β phase at room temperature, the corresponding change in $[V]_{\alpha}$ is below our measurement uncertainty.

When the β phase becomes apparent in the powder bed material above 950 K (677 °C), the vanadium

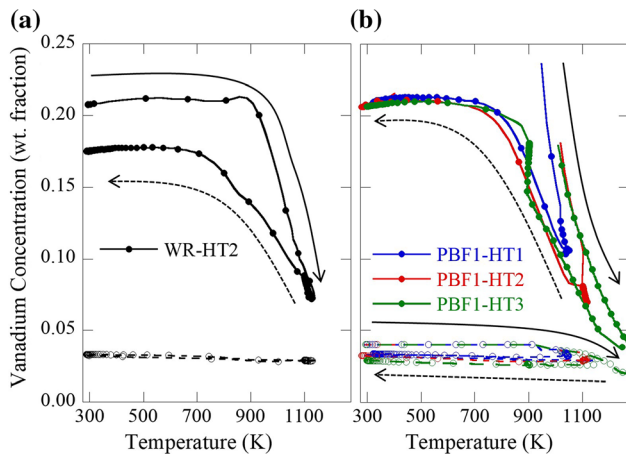


Fig. 13—Vanadium concentration in the α phase (open symbols) and β phase (closed symbols) as a function of PBF of temperature during thermal cycles in the (a) wrought and (b) PBF materials.

concentration in the β phase is roughly 0.2 and decreases rapidly as the β phase fraction increases. When the HT1 soak at 1043 K (770 °C) is reached, $[V]_{\beta}$ has decreased to 0.104 and increases to 0.106 at the end of the soak. At the HT2 soak of 1113 K (840 °C), $[V]_{\beta}$ is initially 0.070 and increases to 0.081 during the two-hour hold. PBF1-HT2 can be directly compared to WR-HT2 as the thermal profiles were nearly identical (Figure 6). The vanadium concentration in the β phase of the wrought material also reached 0.072 when HT2 was reached, but increased to 0.088 during the hold. During HT3, $[V]_{\beta}$ initially follows the same path as HT2 but continues to decrease with increasing temperature. Of course, at the β transus, the vanadium must all be in the β phase and $[V]_{\beta}$ is 0.04.

With cooling from the soak temperature, in each case, the vanadium concentration in the β phase increases rapidly as the β fraction decreases. During the hold at 900 K while cooling from the β transus (HT3), $[V]_{\beta}$ increases isothermally by ~20 pct from 0.146 to 0.181 while v_{β} decreases correspondingly from 0.11 to 0.09. At room temperature, in each case, the vanadium concentration is slightly higher than 0.20, but this is essentially fixed by the constraint that $[V]_{\beta} = 0.04$ at the β transus. $[V]_{\alpha}$ was initially 0.04 and reduces to 0.03 after the heat treatments. For comparison, the vanadium distribution in Shape Metal Deposited (SMD) Ti64 was reported as $[V]_{\alpha} = 0.026$ and $[V]_{\beta} = 0.054$ as deposited and $[V]_{\alpha} = 0.014$ and $[V]_{\beta} = 0.196$ after a β phase thermal cycle.^[15] The cooling rates during SMD are much slower than laser powder bed fusion, accounting for the initial presence of β and differences in vanadium distribution. However, following similar heat treatments above the β transus, the final vanadium distribution is very similar to that found here. Both Simonelli *et al.*^[14] and Xu *et al.*^[18] report manipulation of the martensitic decomposition and, thus, the vanadium distribution through control of process parameters but meaningful comparisons to vanadium concentrations reported therein are difficult because they refer to the as-built condition.

The vanadium concentration in the β phase of the PBF material increases more quickly during cooling than in the wrought material and reaches a higher final concentration upon return to room temperature. As the β to α transformation occurs on cooling, the vanadium diffuses to the remaining β grains which primarily decorate the α grain boundaries. Since the α grains are much smaller in the PBF material, even after the highest heat treatment temperature, than in the wrought material, the β phase vanadium concentration increases more quickly in the PBF material as the distance it must diffuse on average is shorter.

The evolution of the lattice strain excluding thermal expansion coupled with the peak width (Figure 8) and grain structure (Figure 3) now paints a clear picture of the microstructural evolution of the laser powder bed fusion Ti64 during post-build heat treatment. In the as-built condition, the Ti64 is in a single-phase hexagonal close packed (to within our sensitivity) crystal structure with a fine acicular vanadium supersaturated α' microstructure. The dislocation density found from quantitative analysis of the diffraction line shape is very

high, $4.0 \pm 0.5 \times 10^{15} / \text{mm}^2$. Significant macroscopic and intergranular residual stresses are present^[34] in the original build, but the macroscopic residual stresses are presumably released by cutting the small samples for *in situ* heat treatment.^[34]

At 770 K, the dislocation density and the intergranular residual stresses begin to decrease indicating that recovery of dislocations and stress relief happen concurrently. At 913 K, transformation from the α to β phase initiates, continuing until the β transus is reached. This is accompanied by vanadium diffusion from the α phase into the β phase as evidenced by a steady increase in the lattice parameters and/or interplanar spacings of both phases beyond that attributable to thermal expansion. It is interesting that the lattice parameters increase in both phases because the vanadium concentration is decreasing in both phases. Even though vanadium is flowing into the β phase, the vanadium concentration decreases because the amount of β phase increases faster.^[51] The measurements described herein cannot evaluate grain growth *in situ*, but while growth is evident after the lowest temperature heat treatment, much more grain growth is achieved during the β phase heat treatment.

During cooling, the β to α diffusional phase transformation occurs in the PBF material much as it does in the wrought material. As transformation progresses during cooling, vanadium is ejected from the incipient α grains to the vanishing β grains, increasing $[V]_{\beta}$. The transformation rate during cooling and room-temperature β phase fraction of the wrought and powder bed material are similar when cooled at the same rate. However, the vanadium concentration increases much faster in the PBF material, and the final $[V]_{\beta}$ is greater in the PBF material following identical thermal treatments. The smaller α grain size in the PBF material shortens the diffusion path for the vanadium to get to the β grains that decorate the grain boundaries.

V. CONCLUSIONS

In situ X-ray diffraction measurements were completed on Ti-6wt pct Al-4wt pct V (Ti64) material additively manufactured through the powder bed fusion process during post-build heat treatments to monitor the evolution of the as-built metastable microstructure. For comparison, analogous measurements were carried out on traditional wrought material.

As built, the powder bed fusion material is single phase α' , to the resolution of the electron microscopy and X-ray diffraction measurements utilized, has an acicular grain structure, perceived intergranular residual stresses and has a very high dislocation density. With heating, at 770 K (497 °C), the dislocation density and intergranular stress concurrently decrease. At 913 K (640 °C), the β phase becomes apparent and increases in fraction until the transformation is complete at 1281 K (1008 °C). Diffusion of vanadium from the α to the β phase over this range is evident and quantified by changes in the lattice parameters and interatomic spacings of each phase. With cooling, the reverse β to

α phase transformation occurs in both the wrought and powder bed fusion material at the same rate. However, the rate of transformation at the cooling rate of 100 K/min is too fast to allow equilibrium expulsion of the vanadium from the incipient α grains. The vanadium concentration in the β phase of the PBF material increases more rapidly than in the wrought material because the small grains limit the necessary diffusion distance in the powder bed fusion material. While the post-build heat treatment of the PBF material does not quite recover the microstructure of the wrought material, the heat treatment does provide the capability to control the microstructure and, thus, the final properties of the material.

ACKNOWLEDGMENTS

This work was performed under the auspices of the U.S. Department of Energy by Los Alamos National Laboratory under the contract DE-AC52-06NA25396 and by Lawrence Livermore National Laboratory under Contract DE-AC52-07NA27344, and the U.S. Department of Commerce by the National Institute of Standards and Technology. The experimental results of the current work are based upon research conducted at the Cornell High-Energy Synchrotron Source (CHESS), which is supported by the National Science Foundation under award DMR-1332208.

REFERENCES

1. W.E. Frazier: *J. Mater. Eng. Perform.*, 2014, vol. 23 (6), pp. 1917–28.
2. D.D. Gu, W. Meiners, K. Wissenbach, and R. Poprawe: *Int. Mater. Rev.*, 2012, vol. 57 (3), pp. 133–64.
3. B. Berman: *Bus. Horizons*, 2012, vol. 55 (2), pp. 155–62.
4. D. Herzog, V. Seyda, E. Wycisk, and C. Emmelmann: *Acta Mater.*, 2016, vol. 117, pp. 371–92.
5. H.K. Rafi, N.V. Karthik, H. Gong, T.L. Starr, and B.E. Stucker: *J. Mater. Eng. Perform.*, 2013, vol. 22 (12), pp. 3872–83.
6. T. DebRoy, H.L. Wei, J.S. Zuback, T. Mukherjee, J.W. Elmer, J.O. Milewski, A.M. Beese, A. Wilson-Heid, A. De, and W. Zhang: *Prog. Mater. Sci.*, 2018, vol. 92, pp. 112–224.
7. W. Xu, E.W. Lui, A. Pateras, M. Qian, and M. Brandt: *Acta Mater.*, 2017, vol. 125, pp. 390–400.
8. J. Yang, H. Yu, J. Yin, M. Gao, Z. Wang, and X. Zeng: *Mater. Des.*, 2016, vol. 108, pp. 308–18.
9. Y.M. Wang, T. Voisin, J.T. McKeown, J. Ye, N.P. Calta, Z. Li, Z. Zeng, Y. Zhang, W. Chen, T.T. Roehling, R.T. Ott, M.K. Santala, P.J. Depond, M.J. Matthews, A.V. Hamza, and T. Zhu: *Nat. Mater.*, 2017, vol. 17, pp. 63–71.
10. B.M. Morrow, T.J. Lienert, C.M. Knapp, J.O. Sutton, M.J. Brand, R.M. Pacheco, V. Livescu, J.S. Carpenter, and G.T. Gray, III: *Metall. Mater. Trans. A*, 2018, vol. 49A (8), pp. 3637–50.
11. M.J.J. Donachie: *Titanium: A Technical Guide*, 2nd ed., ASM International, Materials Park, OH, 2000.
12. G. Lutjering and J.C. Williams: *Titanium*, Springer, Berlin, 2003.
13. J.W. Elmer, T.A. Palmer, S.S. Babu, and E.D. Specht: *Mater. Sci. Eng. A*, 2005, vol. 391 (1–2), pp. 104–13.
14. M. Simonelli, Y.Y. Tse, and C. Tuck: *J. Mater. Res.*, 2014, vol. 29 (17), pp. 2028–35.
15. A.K. Swarnakar, O. Van der Biest, and B. Baufeld: *J. Alloy Compd.*, 2011, vol. 509 (6), pp. 2723–28.
16. L. Thijs, F. Verhaeghe, T. Craeghs, J. Van Humbeeck, and J.-P. Kruth: *Acta Mater.*, 2010, vol. 58 (9), pp. 3303–12.
17. S. Liu and Y.C. Shin: *Mater. Des.*, 2019, vol. 164, p. 107552.
18. W. Xu, M. Brandt, S. Sun, J. Elambasseril, Q. Liu, K. Latham, K. Xia, and M. Qian: *Acta Mater.*, 2015, vol. 85, pp. 74–84.
19. B. Vrancken, L. Thijs, J.-P. Kruth, and J. Van Humbeeck: *J. Alloy Compd.*, 2012, vol. 541, pp. 177–85.
20. G.M. Ter Haar and T.H. Becker: *Materials* vol. 11(1), p. 146, 2018.
21. E. Brandl and D. Greitemeier: *Mater. Lett.*, 2012, vol. 81, pp. 84–87.
22. C. Zhao, K. Fezzaa, R.W. Cunningham, H. Wen, F. De Carlo, L. Chen, A.D. Rollett, and T. Sun: *Sci. Rep.*, 2017, vol. 7 (1), pp. 1–11.
23. Q. Guo, C. Zhao, L.I. Escano, Z. Young, L. Xiong, K. Fezzaa, W. Everhart, B. Brown, T. Sun, and L. Chen: *Acta Mater.*, 2018, vol. 151, pp. 169–80.
24. C. Kenel, D. Grolimund, J.L. Fife, V.A. Samson, S. Van Petegem, H. Van Swygenhoven, and C. Leinenbach: *Scr. Mater.*, 2016, vol. 114, pp. 117–20.
25. J.W. Elmer, T.A. Palmer, S.S. Babu, and E.D. Specht: *Scr. Mater.*, 2005, vol. 52 (10), pp. 1051–56.
26. J.W. Elmer, T.A. Palmer, and J. Wong: *J. App. Phys.*, 2003, vol. 93 (4), pp. 1941–47.
27. D.W. Brown, A. Losko, J.S. Carpenter, J.C. Cooley, B. Clausen, J. Dahal, P. Kenesei, and J.S. Park: *Metall. Mater. Trans. A*, 2019, vol. 50A (5), pp. 2538–53.
28. A.M. Beese: Microstructure and mechanical properties of AM builds in *Thermo-Mechanical Modeling of Additive Manufacturing*, M. Gouge and P. Michaleris, eds., Elsevier, Butterworth-Heinemann, 2018, pp. 81–92.
29. D.W. Brown, A. Losko, J.S. Carpenter, B. Clausen, J.C. Cooley, V. Livescu, P. Kenesei, J.S. Park, T.J. Stockman, and M. Strantz: *Metall. Mater. Trans. A*, 2020, vol. 51A (3), pp. 1379–94.
30. D.W. Brown, D.P. Adams, L. Balogh, J.S. Carpenter, B. Clausen, V. Livescu, R.M. Martinez, B.M. Morrow, T.A. Palmer, R. Pokharel, M. Strantz, and S.C. Vogel: *Metall. Mater. Trans. A*, 2019, vol. 50A (7), pp. 3399–3413.
31. S.C. Vogel, S. Takajo, M.A. Kumar, E.N. Caspi, A. Pesach, E. Tiferet, and O. Yeheskel: *JOM*, 2018, vol. 70 (9), pp. 1714–22.
32. B. Clausen, D.W. Brown, J.S. Carpenter, K.D. Clarke, A.J. Clarke, S.C. Vogel, J.D. Bernardin, D. Spornjak, and J.M. Thompson: *Mater. Sci. Eng. A*, 2017, vol. 696, pp. 331–40.
33. ISO/ASTM 52900: <https://www.iso.org/obp/ui/#iso:std:iso-astm:52900:dis:ed-2:vl:en>, July 7, 2021.
34. M. Strantz, R.K. Ganeriwala, B. Clausen, T.Q. Phan, L.E. Levine, D. Pagan, W.E. King, N.E. Hodge, and D.W. Brown: *Mater. Lett.*, 2018, vol. 231, pp. 221–24.
35. W. Yinmin, C. Kamath, T. Voisin, and Z. Li: *Rapid Prototyping J.*, 2018, vol. 24 (9), pp. 1469–78.
36. Y.S. Touloukian, R.K. Kirby, R.E. Taylor, and P.D. Desai: *Thermal Expansion: Metallic Elements and Alloys*, Plenum Publishing Company, New York, 1975.
37. J. Zhang, D.W. Brown, B. Clausen, S.C. Vogel, and R.E. Hackenberger: *Metall. Mater. Trans. A*, 2019, vol. 50A (6), pp. 2619–28.
38. H.M. Rietveld: *J. Appl. Cryst.*, 1969, vol. 2, pp. 65–71.
39. L. Lutterotti, S. Matthies, H.-R. Wenk, A.J. Schultz, and J.W. Richardson: *J. Appl. Phys.*, 1997, vol. 81, pp. 594–600.
40. L. Lutterotti, R. Vasin, and H.-R. Wenk: *Powder Differ.*, 2014, vol. 29 (1), pp. 76–84.
41. L. Lutterotti, D. Chateigner, S. Ferrari, and J. Ricote: *Thin Solid Films*, 2004, vol. 450 (1), pp. 34–41.
42. B.H. Toby and R.B. Von Dreele: *J. Appl. Cryst.*, 2013, vol. 46, pp. 544–49.
43. B. Clausen: Report LA-UR 04-6581. Los Alamos National Lab, 2004.
44. A.C. Larson and R.B. Von Dreele: Los Alamos National Lab, 1986.
45. G. Ribarik and T. Ungar: *Mater. Sci. Eng. A*, 2010, vol. 528, pp. 112–21.
46. G. Ribarik, J. Gubicza, and T. Ungar: *Mater. Sci. Eng. A*, 2004, vol. 387, pp. 343–47.
47. D.W. Brown, J.D. Almer, L. Balogh, E.K. Cerreta, B. Clausen, J.P. Escobedo-Diaz, T.A. Sisneros, P.L. Mosbrucker, E.F. Tulk, and S.C. Vogel: *Acta Mater.*, 2014, vol. 67, pp. 383–94.

48. M.R. Daymond: *J. Appl. Phys.*, 2004, vol. 96 (8), pp. 4263–72.
49. D.W. Brown, M.A.M. Bourke, B. Clausen, T.M. Holden, C.N. Tome, and R. Varma: *Metall. Mater. Trans. A*, 2003, vol. 34A (7), pp. 1439–49.
50. T. Voisin, N.P. Caltá, S.A. Khairallah, J.-B. Forien, L. Balogh, R.W. Cunningham, A.D. Rollett, and Y.M. Wang: *Mater. Des.*, 2018, vol. 158, pp. 113–26.
51. J.W. Elmer, T.A. Palmer, S.S. Babu, W. Zhang, and T. DebRoy: *J. Appl. Phys.*, 2004, vol. 95 (12), pp. 8327–39.
52. I.C. Dragomir and T. Ungar: *J. App. Crys.*, 2002, vol. 35, pp. 556–64.
53. M. Strantza, R.K. Ganeriwala, B. Clausen, T.Q. Phan, L.E. Levine, D.C. Pagan, J.P.C. Ruff, W.E. King, N.S. Johnson, R.M. Martinez, V. Anghel, G. Rafailov, D.W. Brown, *Additive Manufacturing*, 2021, vol. Accepted in pp.
54. A.M. Russell and B.A. Cook: *Scr. Mater.*, 1997, vol. 37 (10), pp. 1461–67.
55. L.C. Ming, M.H. Manghnani, and K.W. Katahara: *Acta Metall.*, 1981, vol. 29 (3), pp. 479–85.
56. A.F. Wells: *Structural Inorganic Chemistry*, 3rd ed., Clarendon Press, Oxford, 1962.
57. WebElements, <https://www.webelements.com/iron/physics.html>, 6-13-18.

Publisher's Note Springer Nature remains neutral with regard to jurisdictional claims in published maps and institutional affiliations.